Electronic structure of the neutral silicon-vacancy center in diamond

B. L. Green,[1,*] M. W. Doherty,[2] E. Nako,[1,3] N. B. Manson,[2] U. F. S. D'Haenens-Johansson,[4] S. D. Williams,[5] D. J. Twitchen,[5] and M. E. Newton[1,3]

[1] *Department of Physics, University of Warwick, Coventry, CV4 7AL, UK*

[2] *Laser Physics Centre, Research School of Physics and Engineering, Australian National University, Australian Capital Territory 2601, Australia*

[3] *EPSRC Centre for Doctoral Training in Diamond Science and Technology, UK*

[4] *Gemological Institute of America, 50 W 47th St, New York, NY 10036, USA*

[5] *Element Six Limited, Global Innovation Centre, Fermi Avenue, OX11 0QR, UK*

I. EXPERIMENTAL DETAIL

We have measured SiV^0 in two samples grown by microwave-plasma chemical vapour deposition. The primary sample for the study was intentionally doped with ^{29}Si during growth, with gas phase concentrations of N_2:CH_4= 13.2 ppm and SiH_4:CH_4= 9.7 ppm, and is untreated since growth. The sample contains approximately 70 ppb of $^{29}SiV^0$ and <15 ppb neutral substitutional nitrogen, as measured by electron paramagnetic resonance. The uncompensated boron concentration was measured as less than 10 ppb using infrared absorption spectroscopy. The sample has faces $\langle 1\,\bar{1}\,0\rangle$, $\langle 1\,1\,1\rangle$ and $\langle 1\,1\,\bar{2}\rangle$. The second sample, used for the $^{28}SiV^0$ spectrum in Figure 3b of the main text, was grown with no added nitrogen and SiH_4:CH_4= 0.4 ppm. The sample contains approximately 10 ppb of SiV^0, and is also untreated post-growth.

Photoluminescence experiments were performed in backscatter geometry i.e. $Z(\psi_e\psi_d)\bar{Z}$ in Porto notation, where ψ_e and ψ_d are the excitation and detection E vector, respectively [Fig. 1(a)]. The measurements were completed using a commercial microscope (Renishaw InVia Raman) equipped with a thermoelectrically-cooled silicon CCD. All measurements were performed using excitation at 785 nm (1.58 eV) generated by a laser diode with approximately 30 mW of optical power incident on the sample focused through an achromatic doublet lens (Thorlabs AC254-050-B-ML) to a spot of approximately 20 µm diameter.

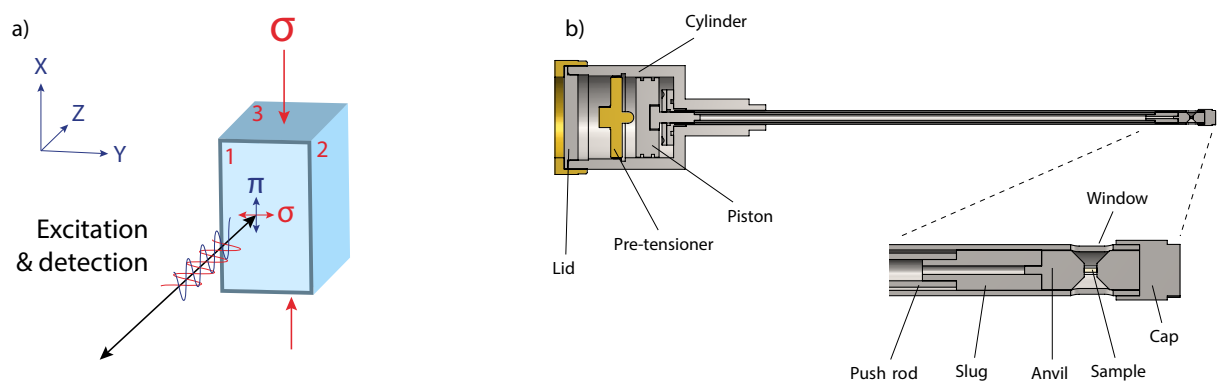

FIG. 1. (a) Geometry for stress experiments: the excitation / detection are backscattered for all measurements. Faces 1, 2, 3 are $[1\,\bar{1}\,\bar{1}]$, $[\bar{1}\,1\,\bar{2}]$, $[1\,1\,0]$ ($[\bar{1}\,1\,\bar{2}]$, $[1\,1\,0]$, $[1\,\bar{1}\,\bar{1}]$) for $\langle 1\,1\,0\rangle$ ($\langle 1\,1\,1\rangle$) stress, respectively. The electric field vector for excitation and detection is either parallel (π) or perpendicular (σ) to the stress axis. (b) Schematic of the home-built ram used to apply uniaxial stress to the sample. The chamber on the left of the cell is filled with nitrogen to a pressure defined by a computer-controller Bronkhorst pressure controller: the pressure is transferred to the sample using a stainless steel ram and hardened steel anvils. For more detail see the description in [1].

Uniaxial stress was applied to the sample using a home-built ram [Fig. 1(b)] driven by high pressure nitrogen gas and controlled by a Bronkhorst flow controller. The stress cell was mounted into an Oxford Instruments Optistat for low temperature measurements. The parameters used to generate the spectra in Figures 1 and 2 of the main text are given in Table I. As discussed in the main text, we find no dependence of the spectra on the input polarization ψ_e [Fig. 2], and so all spectra are presented for both detection polarizations only.

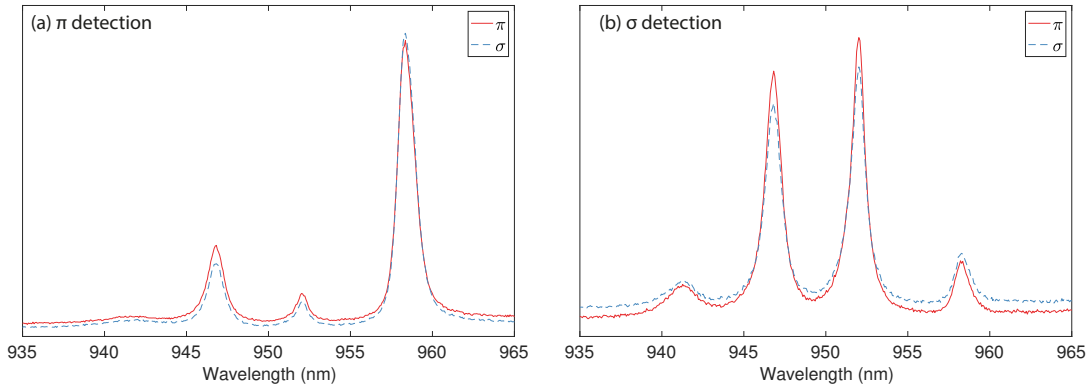

FIG. 2. Comparison of raw spectra collected at an applied ⟨1 1 0⟩ stress of 2.1 GPa. Spectra are given for (a) π detection polarization and (b) σ detection polarization: the two input polarizations are given in each case. No significant difference between input polarizations is visible at this or any other stress value measured.

II. THE MODEL

For a given SiV sub-ensemble under applied stress, the coupled Hamiltonian is

$$H = \begin{pmatrix} W+\alpha' & \gamma^c & \beta^c \\ \gamma^c & \alpha+\beta & \gamma \\ \beta^c & \gamma & \alpha-\beta \end{pmatrix} \tag{1}$$

where α, β, γ (α') describe the response to stress of the E (A) state, β^c and γ^c describe coupling between the two states, and W is the energy difference between the states at zero stress. $\alpha^{(\prime)}$, $\beta^{(c)}$ and $\gamma^{(c)}$ are functions of the state-dependent piezospectroscopic parameters and are linear in applied stress. The eigenenergies of this Hamiltonian can be parameterised as follows (see next section for derivation)

$$\begin{aligned} E(A) =& \frac{1}{2}\left(\alpha+\Delta+W+\alpha'\right) \\ &- \frac{1}{2}\left[\left(\alpha+\Delta-W-\alpha'\right)^2+4\Omega^2\right]^{1/2} \\ E(\Gamma_1^-) =& \alpha-\Delta \\ E(\Gamma_2^-) =& \frac{1}{2}\left(\alpha+\Delta+W+\alpha'\right) \\ &+ \frac{1}{2}\left[\left(\alpha+\Delta-W-\alpha'\right)^2+4\Omega^2\right]^{1/2} \end{aligned} \tag{2}$$

where Δ is the stress splitting of the E level in the absence of the coupling to the A level and Ω is the coupling between the A level and the E state that also has Γ_2^- symmetry under C_{2h} stress. The E orbital sub-states are labeled by their symmetry in the stress-distorted C_{2h} geometric symmetry; the A state is simply labeled A, but as mentioned in the main text corresponds to a state with Γ_2^- symmetry under applied stress. The intensities of the corresponding lines in detection polarization p are

$$\begin{aligned} I_p(A) &= Z^{-1}e^{-E(A)/k_BT}I_{1p}\sin^2\frac{\phi}{2} \\ I_p\left(\Gamma_1^-\right) &= Z^{-1}e^{-E\left(\Gamma_1^-\right)/k_BT}I_{1p} \\ I_p\left(\Gamma_2^-\right) &= Z^{-1}e^{-E\left(\Gamma_2^-\right)/k_BT}I_{2p}\cos^2\frac{\phi}{2} \end{aligned} \tag{3}$$

TABLE I. Model parameter values used to generate the simulation given in the main text. All parameters are in meV GPa^{-1} except W, which is given in meV.

$\mathscr{A}_1$	$\mathscr{A}_2$	$\mathscr{B}$	$\mathscr{C}$	$\mathscr{A}_1'$	$\mathscr{A}_2'$	$\mathscr{B}$	$\mathscr{C}$	W
−0.077	0.93	−1.0	−0.24	0.97	1.1	−4.7	−1.1	−6.8

where I_{1p} and I_{2p} are intensities of p-polarization components of the Γ_1^- and Γ_2^- transitions, $\phi = \arctan \frac{2\Omega}{\alpha+\Delta-W-\alpha'}$ is the angle describing the coupling between the A and the Γ_2^- substate of the E state, and Z is the partition function.

III. DERIVATION OF THE STRESS HAMILTONIAN SOLUTIONS

Let the stress Hamiltonian of A and E states in the absence of coupling be

$$H_{\text{uncoupled}} = \begin{pmatrix} W+\alpha' & 0 & 0 \\ 0 & \alpha+\beta & \gamma \\ 0 & \gamma & \alpha-\beta \end{pmatrix} . \tag{4}$$

The Hamiltonian describing the coupling interaction between the states is

$$H_{\text{coupled}} = \begin{pmatrix} 0 & \gamma^c & \beta^c \\ \gamma^c & 0 & 0 \\ \beta^c & 0 & 0 \end{pmatrix} \tag{5}$$

The eigenbasis of the coupling-free $H_{\text{uncoupled}}$ is

$$\begin{pmatrix} 1 & 0 & 0 \\ 0 & \cos\left[\frac{\theta}{2}\right] & -\sin\left[\frac{\theta}{2}\right] \\ 0 & \sin\left[\frac{\theta}{2}\right] & \cos\left[\frac{\theta}{2}\right] \end{pmatrix} \tag{6}$$

Transforming into this basis, the matrix representation of the total Hamiltonian $H = H_{\text{uncoupled}} + H_{\text{coupled}}$ is

$$H = \begin{pmatrix} W+\alpha' & \gamma^c\cos\left[\frac{\theta}{2}\right]+\beta^c\sin\left[\frac{\theta}{2}\right] & \beta^c\cos\left[\frac{\theta}{2}\right]-\gamma^c\sin\left[\frac{\theta}{2}\right] \\ \gamma^c\cos\left[\frac{\theta}{2}\right]+\beta^c\sin\left[\frac{\theta}{2}\right] & \alpha+\beta\cos[\theta]+\gamma\sin[\theta] & \gamma\cos[\theta]-\beta\sin[\theta] \\ \beta^c\cos\left[\frac{\theta}{2}\right]-\gamma^c\sin\left[\frac{\theta}{2}\right] & \gamma\cos[\theta]-\beta\sin[\theta] & \alpha-\beta\cos[\theta]-\gamma\sin[\theta] \end{pmatrix} \tag{7}$$

The expressions for α, β and γ are defined by the symmetry of the center (D_{3d}), and are given below following [2, 3]:

$$\begin{aligned} \alpha &= \mathscr{A}_1(\sigma_{XX}+\sigma_{YY}+\sigma_{ZZ}) + 2\mathscr{A}_2(\sigma_{YZ}+\sigma_{ZX}+\sigma_{XY}) \\ \beta &= \mathscr{B}(2\sigma_{ZZ}-\sigma_{XX}-\sigma_{YY}) + \mathscr{C}(2\sigma_{XY}-\sigma_{YZ}-\sigma_{ZX}) \\ \gamma &= \sqrt{3}\mathscr{B}(\sigma_{XX}-\sigma_{YY}) + \sqrt{3}\mathscr{C}(\sigma_{YZ}-\sigma_{ZX}) \end{aligned} \tag{8}$$

Here, the σ_{ij} refer to elements of the stress matrix expressed in the crystal axes. α' is defined as α but with $\mathscr{A}_1'$, $\mathscr{A}_2'$ to reflect the different piezospectroscopic response of the doublet and singlet states. Similarly, β^c and γ^c are as β, γ with $\mathscr{B}^c$ and $\mathscr{C}^c$. W is the difference in energy between the doublet and singlet excited states. The reduced matrix elements $\mathscr{A}_1^{(\prime)}$, $\mathscr{A}_2^{(\prime)}$, $\mathscr{B}^{(c)}$, and $\mathscr{C}^{(c)}$ have the same form as given by [4].

We now construct the Hamiltonian for each sub-ensemble for each stress direction.

$\langle 1\,1\,1\rangle$ stress

The angle between the defect symmetry axis z and the applied stress axis $\hat{\boldsymbol{\sigma}}$ is denoted θ_σ. For $\langle 1\,1\,1\rangle$ stress applied to a trigonal defect, we need only consider two cases: the 'unique' orientation with $\theta_\sigma = 0°$; and the three equivalent orientations with $\theta_\sigma = 109°$.

The stress matrix is constructed as $\sigma_{ij} = \sigma(\hat{\boldsymbol{\sigma}}.i) \times (\hat{\boldsymbol{\sigma}}.j)$, where i, j run over the crystal axes X, Y, Z, and is subsequently rotated into each orientation frame. For the representative orientations 1 & 2 [see Table II] with the substitution $\theta = \lim_{x\to\beta} \frac{\gamma}{\beta}$, the Hamiltonian parameters are:

	α	$\beta \equiv \Delta$	γ	α'	$\beta^c \equiv \Omega$	γ^c
0° sub-ensemble	$\sigma(\mathscr{A}_1 + 2\mathscr{A}_2)$	0	0	$\sigma(\mathscr{A}_1' + 2\mathscr{A}_2')$	0	0
109° sub-ensemble	$\sigma(\mathscr{A}_1 - \frac{2}{3}\mathscr{A}_2)$	$\frac{4}{3}\mathscr{C}\sigma$	0	$\sigma(\mathscr{A}_1' - \frac{2}{3}\mathscr{A}_2')$	$\frac{4}{3}\mathscr{C}^c\sigma$	0

TABLE II. The four possible orientations of a trigonal center in a T_d lattice.

	x	y	z
1	$[1\,\bar{1}\,0]$	$[1\,1\,\bar{2}]$	$[1\,1\,1]$
2	$[\bar{1}\,1\,0]$	$[\bar{1}\,\bar{1}\,\bar{2}]$	$[\bar{1}\,\bar{1}\,1]$
3	$[1\,1\,0]$	$[1\,\bar{1}\,2]$	$[1\,\bar{1}\,\bar{1}]$
4	$[\bar{1}\,\bar{1}\,0]$	$[\bar{1}\,1\,2]$	$[\bar{1}\,1\,\bar{1}]$

Finally, the eigenvalues of the resulting Hamiltonian are as above with $\Delta \equiv \beta$ and $\Omega \equiv \beta^c$:

	α	Δ	α'	Ω
0° sub-ensemble	$\sigma\left(\mathscr{A}_1 + 2\mathscr{A}_2\right)$	0	$\sigma\left(\mathscr{A}_1' + 2\mathscr{A}_2'\right)$	0
109° sub-ensemble	$\sigma\left(\mathscr{A}_1' - \frac{2}{3}\mathscr{A}_2'\right)$	$\frac{4}{3}\mathscr{C}\sigma$	$\sigma\left(\mathscr{A}_1' - \frac{2}{3}\mathscr{A}_2'\right)$	$\frac{4}{3}\mathscr{C}^c\sigma$

$\langle 1\,1\,0\rangle$ stress

For $\langle 1\,1\,0\rangle$ applied stress, we need again only consider two cases: the pair of orientations with $\theta_\sigma = 35°$; and the pair of orientations with $\theta_\sigma = 90°$. For the representative orientations 1 & 3 [see Table II], the Hamiltonian parameters are:

	α	$\beta \equiv \Delta$	γ	α'	$\beta^c \equiv \Omega$	γ^c
35° sub-ensemble	$\sigma(\mathscr{A}_1 + \mathscr{A}_2)$	$\sigma(-\mathscr{B} + \mathscr{C})$	0	$\sigma(\mathscr{A}_1' + \mathscr{A}_2')$	$\sigma(-\mathscr{B}^c + \mathscr{C}^c)$	0
90° sub-ensemble	$\sigma(\mathscr{A}_1 - \mathscr{A}_2)$	$\sigma(-\mathscr{B} - \mathscr{C})$	0	$\sigma(\mathscr{A}_1' - \mathscr{A}_2')$	$\sigma(-\mathscr{B}^c - \mathscr{C}^c)$	0

As found in the $\langle 1\,1\,1\rangle$ case, $\Delta \equiv \beta$ and $\Omega \equiv \beta^c$.

IV. INTENSITIES OF STRESS-SPLIT TRANSITIONS

As discussed above and in the main text, for photoluminescence stress measurements performed with an ionizing input beam, the spectra are essentially invariant to input polarization and therefore the expected intensities therefore reduce to the case encountered in absorption measurements.

The expressions for the intensities given in the model require the intensities of each transition at zero stress in the experimental geometry. The analytical values have been calculated in several places [4, 5]. However, the sample used in our experiment has $\{1\,1\,1\}$, $\{1\,1\,\bar{2}\}$ and $\{1\,\bar{1}\,0\}$ faces: the standard tables give intensities for $\langle 1\,1\,0\rangle$ or $\langle 0\,0\,1\rangle$ readout under $\langle 1\,\bar{1}\,0\rangle$ stress. In Table III we give the zero-stress intensities for both $\langle 1\,1\,1\rangle$ and $\langle 1\,1\,0\rangle$ stress, including intensities of transitions when measured with detection polarization $\psi_d \| \langle 1\,1\,\bar{2}\rangle$ under $\boldsymbol{\sigma} \| \langle 1\,1\,0\rangle$, as found in our experiment.

TABLE III. Analytical intensities for different detection polarizations for an $E \leftrightarrow A_2$ transition at an inversion-symmetric trigonal center. The table has been adapted from [6] to apply to an E_u level of a D_{3d} defect using relationships between the D_{3d} and C_{3v} point groups and their C_{2h} and C_s sub groups under stress. For $\langle 1\,1\,0\rangle$ stress, the σ polarization values are calculated for a perpendicular direction of $\langle 1\,1\,\bar{2}\rangle$, as employed in our experiment.

Stress	Orientation	Sym.	Energy	π	σ
$\langle 1\,1\,1\rangle$	① 0°	E_X, E_Y	$\mathscr{A}_1 + 2\mathscr{A}_2$	0	1
	②, ③, ④ 70° (XZ)	E_X (Γ_2^-)	$\mathscr{A}_1 - \frac{2}{3}\mathscr{A}_2 + \frac{4}{3}\mathscr{C}$	0	$\frac{3}{2}$
		E_Y (Γ_1^-)	$\mathscr{A}_1 - \frac{2}{3}\mathscr{A}_2 - \frac{4}{3}\mathscr{C}$	$\frac{8}{3}$	$\frac{1}{6}$
$\langle 1\,1\,0\rangle$	①, ② 35° (XZ)	E_X (Γ_2^-)	$\mathscr{A}_1 + \mathscr{A}_2 - \mathscr{B} + \mathscr{C}$	0	$\frac{2}{3}$
		E_Y (Γ_1^-)	$\mathscr{A}_1 + \mathscr{A}_2 + \mathscr{B} - \mathscr{C}$	$\frac{2}{3}$	$\frac{8}{9}$
	③, ④ 90° (YZ)	E_X (Γ_2^-)	$\mathscr{A}_1 - \mathscr{A}_2 - \mathscr{B} - \mathscr{C}$	2	0
		E_Y (Γ_1^-)	$\mathscr{A}_1 - \mathscr{A}_2 + \mathscr{B} + \mathscr{C}$	0	$\frac{10}{9}$

V. ⟨1 1 1⟩ STRESS DATA

The data presented in the main text give the experimental data for both ⟨1 1 0⟩ and ⟨1 1 1⟩ applied uniaxial stresses, in addition to the model output for the ⟨1 1 0⟩ case. In Fig. 3, we give the equivalent comparison between the experimental and model data for the ⟨1 1 1⟩ case.

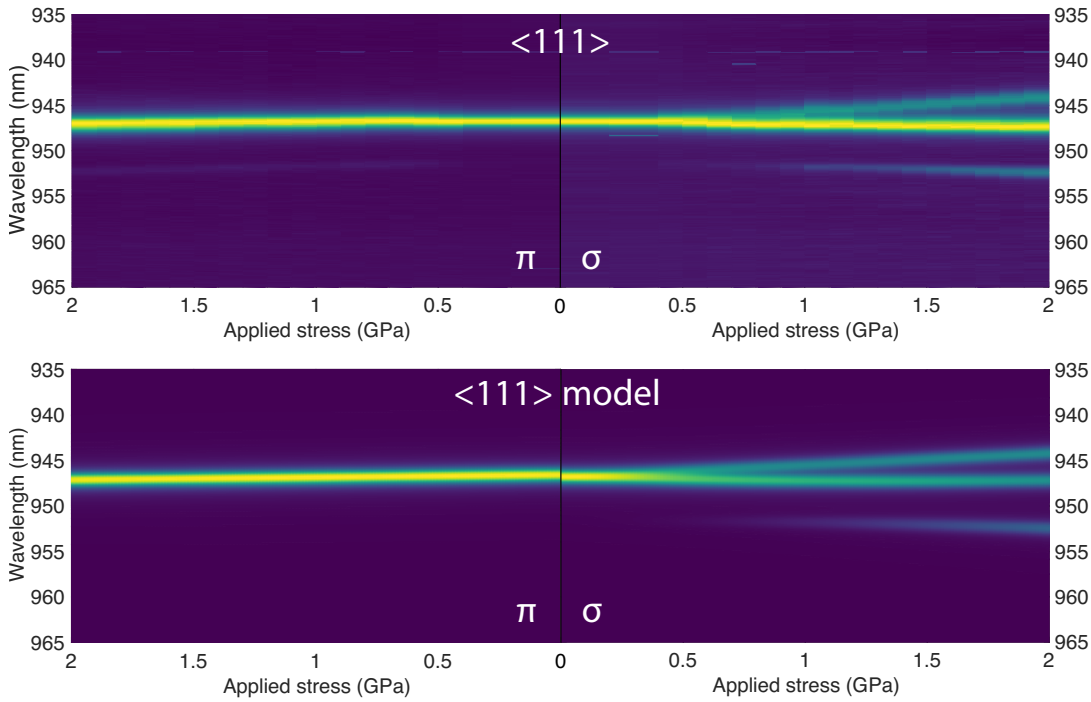

FIG. 3. Top: SiV^0 photoluminescence spectra collected at 80 K as a function of applied stress along ⟨1 1 1⟩. Bottom: The output of the model generated using the parameters given in Table I — equivalent to the bottom panel of Fig 1 of the main text, but for $\sigma \| \langle 1\,1\,1 \rangle$ rather than $\sigma \| \langle 1\,1\,0 \rangle$.

VI. TEMPERATURE DEPENDENCE

The fitted intensities of the different transitions are given as a function of temperature in Fig. 2b of the main text. The raw spectra are included in Fig 4(a) for comparison. The only transitions which increase in intensity with decreasing temperature are those we associate with emission from the $^3A_{2u}$ state: the total intensity from the $^3A_{2u}$ state increases at the expense of the ^3E_u emission intensity [Fig 4(b)].

VII. 976 NM TRANSITION

As described in the main text, the qualitative behavior of the 946 nm and 976 nm transitions is identical. However, a small additional transition appears in certain excitation-detection combinations, namely $\pi\pi$ and $\sigma\sigma$ [Fig 5]. As no other features of the 946 nm system are sensitive to input polarization in these measurements, we attribute this additional peak to an unrelated feature.

VIII. SPIN POLARIZATION MECHANISM

The electronic structure of SiV^0 is complex, with three and six electronic states arising from the first two lowest-energy electronic configurations e_g^2 and $e_u e_g$, respectively. Considering only symmetric A_{1g} phonons, the first-order intersystem crossings (ISC) from the triplet manifold to the singlet manifold are given in Fig. 6. Spin-selective decay may occur from either $m_s = 0$ or $ms = \pm 1$ of $^3A_{2u}$ depending on whether the $^1A_{1u}$ or ^1E_u level is lower in energy

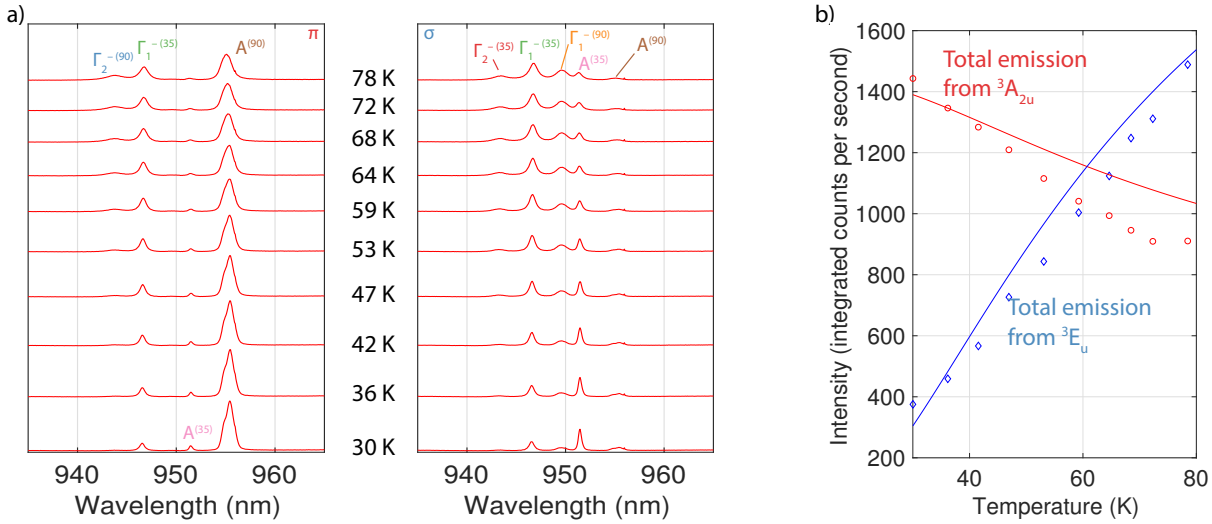

FIG. 4. (a) Raw spectra collected for an applied uniaxial ⟨1 1 0⟩ stress of 1.3 GPa for π and σ detection polarizations. In both polarizations the only transitions which gain intensity are those related to the lower-lying $^3A_{2u}$ state. The transitions are labelled as in Fig 2 of the main text. (b) The total intensity of the transitions measured from the $^3A_{2u}$ and ^3E_u states for experiment (dots) and from the model (solid lines). The intensities have been normalized as in Fig. 2 of the main text.

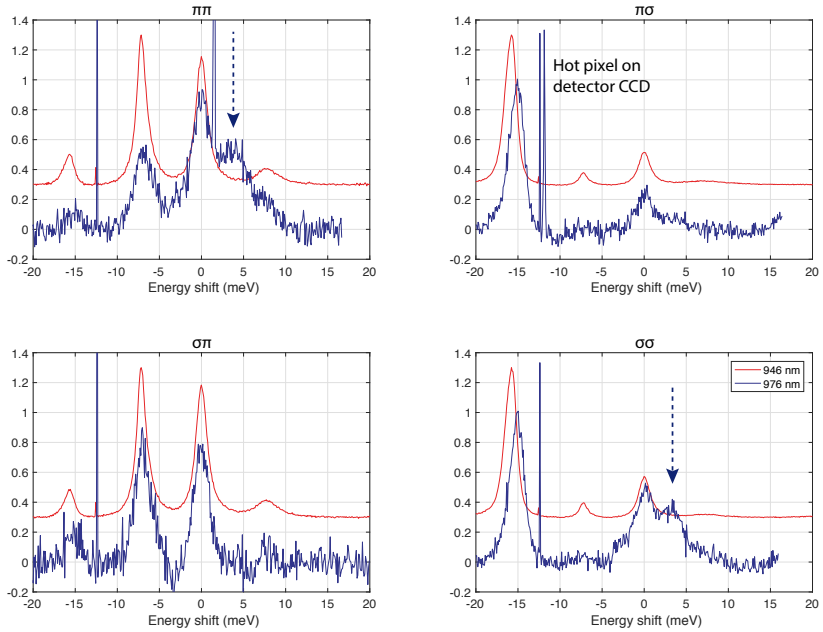

FIG. 5. Comparison of 946 nm spectra (red) with 976 nm spectra under 2.1 GPa of applied ⟨1 1 0⟩ stress. The spectra are labelled with excitation and detection polarization. In each case, spectra are essentially identical except for the feature marked with an arrow in the $\pi\pi$ and $\sigma\sigma$ spectra. No other feature of the SiV^0 system is sensitive to input polarization and therefore we assign it to an unrelated defect emitting close to the 976 nm transition.

than $^3A_{2u}$. This spin-selective decay will yield spin-readout and ODMR as long as the decay rate is comparable to the $^3A_{2u}$ radiative rate and the passage through the singlet levels back to the ground $^3A_{2u}$ is slow compared to the radiative rate.

If the $^1A_{1g}$ is the lowest singlet in the ground configuration, then there will also be spin-selective repopulation of the ground $^3A_{2g}$. If this is the case and the $^1A_{1u}$ is the level lower than the $^3A_{2u}$ in the excited configuration, then the combined ISC processes will not flip the electron spin and so yield inefficient spin-polarization. If the ^1E_u is instead the lower singlet level, then the combined ISC processes will yield a spin-flip and thus efficiently polarize the spin.

If the ^1E_g is the lowest singlet in the ground configuration, then the repopulation of the $^3A_{2g}$ occurs via second-order

mechanisms. This makes it much harder to judge whether or not the repopulation has a net spin-selectivity.

Greater understanding of the ordering of the singlet levels is required before further analysis of the optical spin-polarization and readout mechanism can be performed.

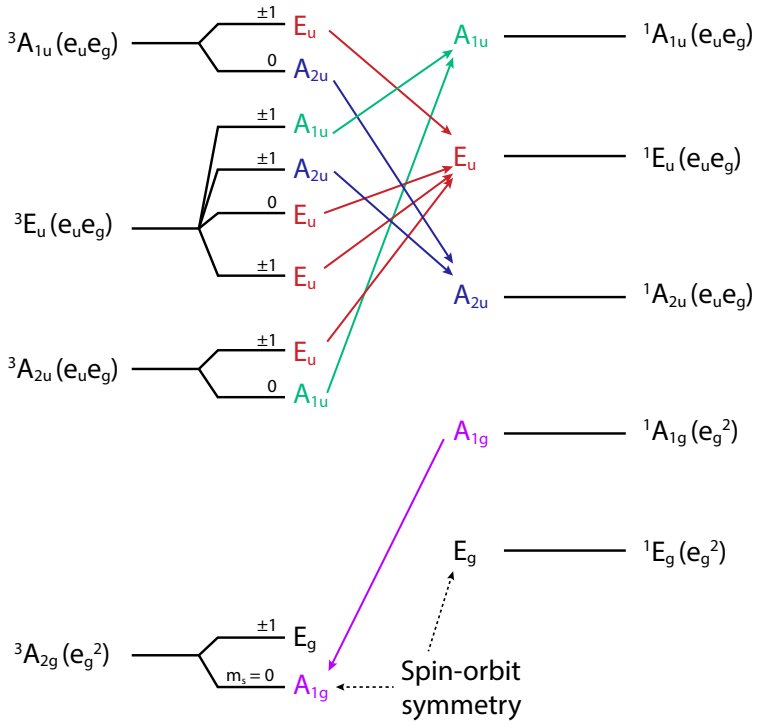

FIG. 6. First-order intersystem crossings involving only A_{1g} phonons. The electronic symmetries are given on the far left and right of the figure, with the spin-orbit symmetry given in the center. Coulomb repulsion has been used to order the triplets relative to each other, and the singlets relative to each other: the ordering between singlets and triplets is not known. The configuration interaction has not been accounted for and may result in different ordering to the one presented. In the case of SiV^0, we anticipate configuration interactions occurring between the first and second excited configurations; however, the second excited configuration will be extremely complex and hence the possible configuration interactions have not been mapped out. Thus, the ordering of the singlets is still an open question.

* b.green@warwick.ac.uk; Corresponding Author

[1] M. W. Dale, *Colour centres on demand in diamond*, Ph.D. thesis, University of Warwick (2015).
[2] A. E. Hughes and W. A. Runciman, Proc. Phys. Soc. **90**, 827 (1967).
[3] G. Davies, J. Phys. C Solid State Phys. **12**, 2551 (1979).
[4] G. Davies and M. E. R. Hamer, Proc. R. Soc. London Ser. A **348**, 285 (1976).
[5] K. Mohammed, G. Davies, and A. T. Collins, J. Phys. C Solid State Phys. **15**, 2779 (1982).
[6] L. J. Rogers, M. W. Doherty, M. S. J. Barson, S. Onoda, T. Ohshima, and N. B. Manson, New J. Phys. **17**, 013048 (2015).